Available online at www.sciencedirect.com

jmr&t Journal of Materials Research and Technology

journal homepage: www.elsevier.com/locate/jmrt

Evaluating the efficacy of alternative small scale test methodologies in deriving the mechanical properties of additive manufactured materials

R.J. Lancaster[*], *N.C. Barnard*, *B. Haigh*, *E.E. Sackett*, *P.E. May*, *R.J. Douglas*, *D. Britton*, *S.P. Jeffs*

Institute of Structural Materials, College of Engineering, Bay Campus, Swansea University, Swansea, SA1 8EN, United Kingdom

ARTICLE INFO

Article history:
Received 18 August 2023
Accepted 21 September 2023
Available online 26 September 2023

Keywords:
Small-scale testing
Additive manufacturing
Small punch
Shear punch
Nano-indentation
Profilometry based indentation plastometry

ABSTRACT

With the continuous drive of the aerospace industry to implement additive manufactured (AM) components into the next generation of aero-engines, to benefit from the near net shape and weight saving potential that the technology has to offer, the requirement to understand their mechanical performance is also rising in parallel. This is further complicated by the highly localised and transient micro/macro structures that AM produced parts typically possess, raising a question mark over the suitability of more traditional mechanical test approaches where the bulk properties are heavily influenced by the presence of a single defect. As such, alternative experimental approaches, capable of establishing the properties of smaller more intricate structures and geometrically representative microstructures and cross sections, needs to be considered for process parameter down-selection. This paper will explore the suitability of several alternative mechanical test methodologies in characterising the mechanical behaviour of a nickel based superalloy, Inconel 718 (IN718), produced by laser powder bed fusion (LPBF), and establish which results correlate most favourably to those generated through more conventional means. For the first time, results will be presented from several mechanical test methodologies including small punch, shear punch, hardness, nano-indentation and profilometry based indentation plastometry experiments; a set of mechanical test approaches that have yet to be directly compared and discussed in a single study on an additively manufactured material. Findings will be supported by advanced microscopy in the form of field emission SEM and crystallographic texture maps produced through electron back-scattered diffraction.

1. Introduction

Additive manufacturing (AM) is a modern process of component manufacture and repair that has advanced considerably over the past 20 years owing to its potential to improve several beneficial factors including lean manufacture, reduced material wastage and the capability to design complex geometries for a diverse range of industrial applications. To date, AM has seen uptake in the aerospace [1], automotive [2],

* Corresponding author.
E-mail address: r.j.lancaster@swansea.ac.uk (R.J. Lancaster).
https://doi.org/10.1016/j.jmrt.2023.09.224

biomedical [3] and nuclear [4] sectors, providing engineers greater freedom in component design [5] and the ability to repair intricate and complex geometries in-situ [6].

However, AM structures are highly intricate due to the transient micro- and macro-structures which are readily produced through additive technologies, resulting from the layer-by-layer melting and re-melting of subsequent layers of powder, which in turn promotes heavily textured, epitaxial grain growth leading to anisotropic morphologies and mechanical properties [7]. AM users will typically wish to determine several key parameters before deciding if a material (in the context of AM, defined by a particular build strategy, post-build treatment, and composition) are sufficient for the intended application. Yet, many authors have discussed the numerous difficulties in establishing appropriate test methodologies for a mechanical assessment due to these highly transient structures, build discontinuity features, and the inherent lack of consistency in the desired final component [8]. Traditionally, conventional uniaxial mechanical test methods would be employed to provide a holistic and overarching characterisation of a material and/or component, but these methods are somewhat limited towards establishing bulk properties. In terms of characterising localised and discrete regions of a component, where the volume constraints of the features are of most interest and there is less mechanical dependency on the presence of a single process induced defective feature, smaller scale mechanical test methods should be considered.

One of the most prominent small scale test methods is the small punch tensile (SP) test. The SP test consists of a miniature disc sample that is subjected to an applied compressive force under a constant rate of displacement, transferred through a hemispherical punch indenter onto the upper surface of the disc, forcing the material through a receiving hole. Recently, the SP test has found use in characterising the mechanical behaviour of AM materials, for example by sampling a series of different laser powder bed fusion (LPBF) process parameter sets and providing an indication of the optimal conditions for the manufacture of alternatively angled CM247LC plates [9]. Furthermore, it has been used to investigate the influence of different post process treatments on the mechanical response of LPBF C263 [10].

Previous research studies have proposed several different empirical methods of correlating SP generated results to uniaxial tensile properties [11–13]. Much of the work has focused on estimating ultimate tensile stress, σ_{UTS}, with the maximum force, F_{MAX}, from a SP generated force-deflection (*F*-*d*) curve, and yield strength, σ_y, with an equivalent yield force, or F_e, from an SP curve. Whereas many of the correlations were found to be material specific, Garcia et al. sampled a diverse range of metallic materials and derived several parameters from the SP test curve to correlate F_e with σ_y. They found that a favourable correlation was derived when F_e was defined as the crossing point between the SP curve and a straight line parallel to the initial slope of the graph, with an offset d of thickness (*t*)/10. Yet, a stronger correlation was found when estimating σ_{UTS} with F_{MAX}. In this study, F_{MAX} was normalised by dividing by the initial thickness of the SP disc (*t*) and the d value at F_{MAX}. However despite this, the relationships that were employed to correlate tensile elongation and d at F_{MAX} were generally poor [14]. Related findings were found by Lancaster et al. [15] who adopted the same methodology of defining F_e to derive an equivalent σ_y value when characterising the SP response of aluminium, copper, stainless steel, Inconel718 (IN718) and Ti–6Al–4V. Based on a series of five SP and uniaxial tests on each material, a coefficient of determination (R^2) value of 0.9292 was achieved when dividing F_e by the thickness of the disc squared, and correlating this to uniaxial proof stress, σ_{PS}. Similar success was found when deriving σ_{UTS} from F_{MAX} values; when F_{MAX} is divided by the disc thickness multiplied by the deflection at F_{MAX} value. This produced an R^2 value of 0.927 [15].

Over the past 20 years, a similar experimental approach to the SP test has been developed in the form of the shear punch (ShP) test. Like the SP test, the ShP test is also capable of determining mechanical properties from a miniature disc specimen, but through penetrating a flat-ended punch indenter through the central region of the disc under an applied load, deforming the disc via pure shear. Hankin et al. [16] determined that the true multiaxial, non-uniform stress state experienced in a ShP test is a relatively uniform mode of shear, with a small compressive stress. To promote shear deformation on a disc specimen, high precision and a tight tolerance is required for both the diameter of the flat-ended punch indenter and the receiving hole in which the material is forced through. These are typically 2.49 mm for the punch and 2.51 mm for the receiving hole. With such dimensions, shear stress (τ) can be calculated using through Eq. (1):

$$\tau = \frac{F}{2\pi r_{avg} t} \tag{1}$$

where *F* is the punch load and r_{avg} is the average of the radius of the punch head and the radius of the receiving hole ($r_{avg} = r_{punch} + r_{die}/2$).

In a similar manner to the SP test, in a ShP test, data is collected regarding the crosshead movement (displacement), the residual deflection on the underside of the disc (deflection) and readings of the corresponding force values required to maintain the designated displacement rate employed. This enables a *F*-*d* curve to be derived, akin to SP testing, which can subsequently be reconfigured into a τ-*d* curve through using Eq. (1). The τ-*d* curve is more relatable to a σ-ε curve generated from a uniaxial tensile test, in that there are several distinguishable deformation stages that can be readily identified. These include an initial period of elastic behaviour which continues until it reaches a yield point, followed by (for a relatively ductile material) a more prolonged stage of plastic deformation until an ultimate load is reached, with fracture occurring shortly after. Given the similarities, a value for maximum shear stress (τ_{USS}), similar to σ_{UTS}, can be readily identified and the two properties have previously been successfully correlated by different sources [15,17]. However, the yield point, otherwise recognised as shear yield stress (τ_y), is less easily defined.

There have been several studies into shear punch testing across a range of material types that can be collated to further aid and strengthen the empirical correlations [15,17–19]. Guduru et al. [17] characterised the mechanical properties of nanocrystalline materials and found that by normalising the d values with the original specimen thickness (*t*), a master curve could be derived that was essentially independent of the

starting disc thickness [17]. More recently, Lancaster et al. employed the method on a range of wrought metallic materials to determine empirical correlations. In this research, a *t*/*100* offset was adopted to determine τ_{PS}, from which σ_{PS} values could be correlated [15]. However, despite the increasing usage of this test approach, there is currently no available literature where the ShP test has been applied to additively manufactured materials.

Profilometry-based Indentation Plastometry (PIP) is a recently developed mechanical testing methodology that offers a unique capability of deriving stress-strain data from a highly localised region. Developed by Plastometrex Ltd., the test method uses instrumented indentation combined with an iterative FE simulation of the indentation procedure, where the plasticity parameters (in terms of a constitutive law) are regularly and repeatedly changed until an optimum agreement is reached between experimental and predicted outcomes. Typically, the tested volume should include a multi-grain morphology which necessitates the need for an indenter radius in the order of 1 mm, and the applied load to be extended into the kN range. Therefore, the test method is unsuitable for nano level investigations [20]. PIP has previously been used to examine the properties of AM materials [20] in the form of the Ni based superalloy ABD-850AM, manufactured by LPBF. In this research, a series of PIP indentations were made on the two alternative faces of vertically and horizontally built LPBF samples, and compared against the results generated through uniaxial tensile tests. The PIP results were used to infer true stress-true strain relationships, enabling a predicted nominal stress-nominal strain curve as would be typically found from a standard uniaxial tensile test. From this, the authors found that the Young's modulus (*E*), σ_{UTS} and σ_y values were all higher on the X–Y plane as opposed to the X–Z plane, thus the test method suitably recognised the levels of anisotropy in the structures. However, the indentation derived nominal stress-nominal strain curve appeared to follow the behaviour of the horizontally built LPBF material, since the indentation outcome is directionally averaged [20].

Nanoindentation is a long established technique which has been used to determine material properties, with much understanding regarding material and tip interactions previously discussed [21,22]. More recently nanoindentation methods have been used in quantifying the mechanical properties of IN718, for understanding the presence of residual stresses [23], characterising the service related properties of the alloy in the additive form [24] and in understanding the role of microstructure in pileup formation of LPBF IN718 [25].

Following on from these studies, this paper will now discuss the application and suitability of these mechanical test approaches in deriving tensile properties of laser powder bed fused IN718, a precipitation strengthened Ni based superalloy. This will include small punch, shear punch, Vickers hardness, nano-indentation and profilometry-based indentation plastometry based testing; mechanical test approaches that have yet to be directly compared and discussed in a single study in the open literature. This research will discuss how the data generated through these methods correlate with more traditionally recognised uniaxial tensile properties and the resulting behaviours will also be linked to the underlying microstructural features in the different alloy variants.

2. Experimental methods

2.1. Material

Laser powder bed fused (LPBF) IN718 cylinders were built on an EOS M290 machine with a volumetric energy density of 67.47 J/mm^3. The cylinders were built from virgin gas atomised powder with the composition given in Table 1. The powder size distribution values were D_{10} = 19.1 μm, D_{50} = 32.9 μm and D_{90} = 55.1 μm. A total of ten cylinders were built via LPBF, five of which were manufactured in the vertical (90°) orientation, and five in the horizontal (0°) orientation, as displayed in Fig. 1. The dimensions of the cylinders in the as-built condition were 73 mm in length and 20 mm in diameter, and were subjected to a standard post-manufacture AMS 5664 heat treatment, which consisted of a solution heat treatment followed by ageing. For the initial solution heat treatment, the cylinders were heated to 1066 °C, held for 1 h, and then quenched in argon. The second stage ageing heat treatment enabled the precipitation of the secondary strengthening phases, such as γ′, MC carbides and δ phase. This included a two-step process, involving heating to 760 ± 10 °C for 10 h, followed by 649 ± 8 °C for 8 h, with the time taken to ramp down and stabilise between the two steps being 1 h 50 min. Post treatment, the cylinders were machined into uniaxial tensile specimens. For comparative purposes, the wrought equivalent of the alloy was also studied, with the composition displayed in Table 2. The wrought material was solution annealed at 965 °C for 1 h, followed by air cooling to room temperature. The main compositional difference between the two alloy variants is the presence of Ta in the LPBF material. Ta is usually added, in addition to Al, Ti and Nb, to promote precipitation of secondary strengthening phases such as Ni_3(Al,Nb,Ti,Ta), recognised as γ'.

2.2. Mechanical test methods

2.2.1. Test specimens

A series of five uniaxial tensile specimens were manufactured from cylindrical rods from the wrought version of the alloy, whilst five LPBF specimens were manufactured in the vertical and horizontal build orientations respectively, according to the process parameters and specifications documented previously. All tensile specimens were manufactured in accordance with ASTM E8-04 [26] and finished with a circumferential polish. The

Table 1 – LPBF IN718 virgin powder composition.

Element	Ni	Fe	Cr	Nb + Ta	Mo	Ti	Al	C, S, Cu, Mn, Si, Co, Cu, B, N
wt%	Bal	17.6	18.8	5.4	3.1	1.03	0.52	Trace

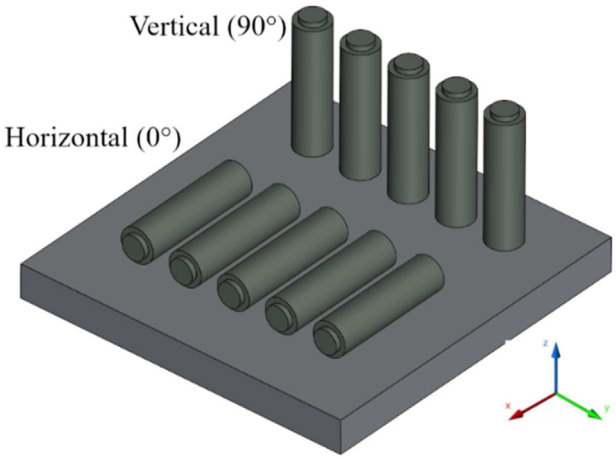

Fig. 1 – Schematic of build plate design with definition of build orientations.

dimensions are given in Fig. 2a. Ten disc specimens (five for SP and five for ShP testing) were then extracted perpendicularly from the same stock of wrought material by reducing the diameter of the cylinders to φ 8 mm and sectioning slices approximately 800 μm in thickness. Likewise, SP and ShP discs from the two LPBF build orientations were extracted from the threaded regions of tested uniaxial tensile specimens, which were also turned down to φ 8 mm prior to sectioning. Disc specimens were then produced by subjecting the material blanks to successive grinding and polishing procedures on both specimen faces, using finer silicon carbide abrasive papers until the required specimen thickness of 500 μm ± 5 μm with a 1200 grit finish (Fig. 2b) was achieved. Such directives follow the recommendations defined in the international standards for SP testing [27,28].

For Vickers hardness, nano-indentation and PIP testing, sections of material were removed from the threaded regions of the uniaxial test specimens to reveal both the X–Y and X–Z planes for the two LPBF build orientations, and the X–Y plane for the wrought material. In each case, the minimum size of the samples was 15 mm (width) x 15 mm (breadth) x 5 mm (depth), exceeding the dimensions stated for PIP by [29]. The material samples were then metallographically prepared using standard mounting, grinding, and polishing procedures, from which indentations could be made on the same sections of material.

2.2.2. *Uniaxial tensile testing*

Uniaxial tensile tests were performed on a Dartec 100 kN electric screw test machine, with Dartec 9610 control system and Dartec Wokshop 96 software. For all tensile tests, a constant strain rate of 0.005 mm min^{-1} was used until the yield strength was exceeded, upon which a second strain rate of 0.05 mm min^{-1} was employed until failure. All test procedures adhered to ASTM E8-04 [26], with 25 data points recorded per second and strain measured through a 12 mm extensometer. All tests were performed in a controlled laboratory temperature of 21 °C. Yield strength was determined by the offset method defined in ASTM E8-04, and elongation was determined after fracture according to the same standard [26].

Table 2 – Wrought IN718 composition.

Element	Ni	Fe	Cr	Nb	Mo	Ti	Al	C, S, Cu
wt%	Bal	19	19	4.8	3	0.86	0.60	Trace

2.2.3. *Small punch tensile (SP) and shear punch tensile (ShP) testing*

SP and ShP tests were performed using a bespoke in-house designed jig assembly, as previously reported in [10]. The jig assembly locates into a 5 kN electric screw test machine and comprises of an upper (2) and lower die (4) set to clamp the miniature disc (3). For SP, the receiving hole is φ4 mm, whilst for the ShP, the equivalent dimension is φ2.51 mm. Both of these dimensions are depicted in Fig. 3. For SP testing, the punch indenter consisted of a φ2.5 mm hemispherical punch end, whilst for ShP, the flat-ended punch had a φ2.49 mm ($w = 10$ μm). Both die sets and punch geometries were manufactured from Nimonic 90. The dimensions of the test equipment used for ShP testing were consistent with those employed in previous studies [15,17].

In both test approaches, deflection measurements were recorded from an adapted transducer rod which connects the centre of the underneath surface of the specimen to a linear variable displacement transducer (LVDT), in addition to readings of the displacement behaviour recorded from the crosshead movement and the corresponding force measurements. All tests were performed in accordance with the EN and ASTM standards for SP testing [27,28], under a crosshead displacement rate of 0.5 mm min^{-1}. Each experiment was performed at ambient room temperature in a controlled laboratory environment (21 °C).

2.2.4. *Profilometry-based indentation plastometry (PIP) testing*

The PIP indentations were made with a silicon nitride spherical indenter (radius 0.5 mm), applying forces of 759 N and 1139 N (in the same location), from which a profile could be analysed and measured after each loading application. The loads used in this technique are determined within the control software by a proprietary algorithm to achieve an indentation depth that corresponds to 10–18% of the indenter radius, further allowing the application of an inverse procedure to describe the material response. An in-built contacting stylus with a depth resolution of 1 μm then scanned each respective indentation in two perpendicular directions, both of which travelled through the central region of the indentations. Tilt correction functions were then applied to the collected raw data automatically, using the machine's software control, based on the far-field parts of the scan being parallel. A set of plasticity parameter values, previously derived in [30,31] were then employed during simulation of the tensile test. Further detail on the PIP procedure is also detailed in [20]. PIP tests were performed on the X–Z and X–Y faces of the vertical and horizontal LPBF samples respectively, whilst a further test was completed on the X–Y face of the wrought material.

2.2.5. *Vickers hardness (H_v) testing*

Vickers hardness (H_v) tests were performed on a Struers Durmain-40 machine. A series of 25 hardness indents were

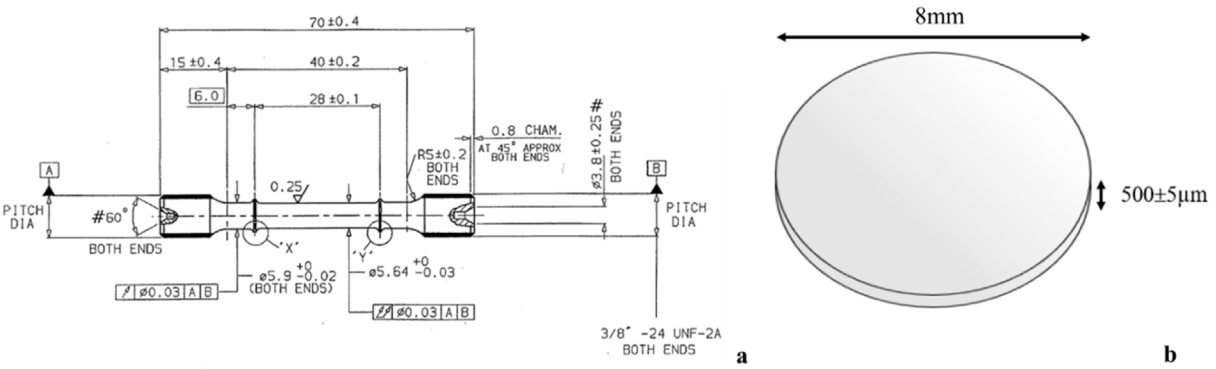

Fig. 2 – Test piece geometry for (a) Uniaxial tensile and (b) Small punch and shear punch testing.

performed in a 5 x 5 configuration, separated by 1 mm spacing, under a force of 1 kgf and dwell time of 10 s. Similar to the PIP experiments, H_V indents were made on the X–Z and X–Y faces of the vertical and horizontal LPBF samples respectively, whilst a further 25 indents were made on the X–Y face of the wrought material.

2.2.6. *Nano-indentation*

Localised hardness behaviour was measured via instrumented indentation tests (nanoindentations) performed on the same 0.04 µm finished specimens as those used for PIP and Vickers hardness testing. Nanoindentation tests were performed using a Hysitron Ti 950 TriboIndenter (Bruker Corp.) machine equipped with a Berkovich diamond tip. A steel disk was attached using a thin layer of cyanoacrylate to the bottom of the mounted sample and secured using a magnetic base. An array of incremental loading single indents were utilised to assess a suitable load and spacing, and to minimise cross-interaction of adjacent indentation strain fields, as per ASTM standards [32]. XPM was used to produce a 10 x 10 array and chained together to produce an indent size map consisting of 400 indents. A peak load of 2000 µN with a 3 µm spacing was used throughout. The unloading curves were analysed using methods previously described by Oliver [21], with the upper 10% and lower 50% disregarded for curve fitting, as per ASTM standards [32]. In-situ scanning probe microscopy (SPM) was used to measure and characterise the indents.

2.3. *Microscopy*

Microstructural analysis using Electron Backscatter Diffraction (EBSD) was conducted on a Hitachi SU3500 scanning electron microscope (SEM) operated at 20 kV. EBSD scans were recorded with a 0.25 µm step size at ×350 magnification across an approximate area of 320 µm × 320 µm using Channel 5 Tango software. The degree of recrystallisation was determined in the material samples by measuring the misorientation distribution and calculated on an area basis using the grain orientation spread (GOS) function in HKL Channel 5. If the orientation spread was less than 2° then the grains were classified as recrystallised. In other studies, this critical internal misorientation angle was used, and if a grain was composed of subgrains with internal misorientations of under 2° but the misorientation from subgrain to subgrain was above 2°, then the grain was classified as substructured [33,34]. This has not been considered here. High resolution imagery and chemical composition of the secondary phases were collected using a JEOL 7800F Field Emission Gun (FEG) SEM along with Energy Dispersive X-ray Spectroscopy (EDS) via an Oxford Instruments SMax 50.

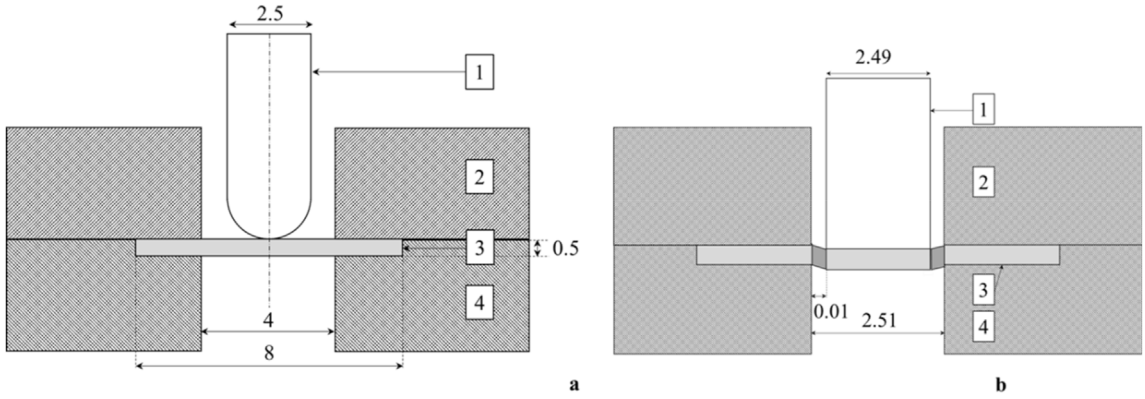

Fig. 3 – Schematic of (a) small punch tensile, and (b) shear punch tensile test assemblies.

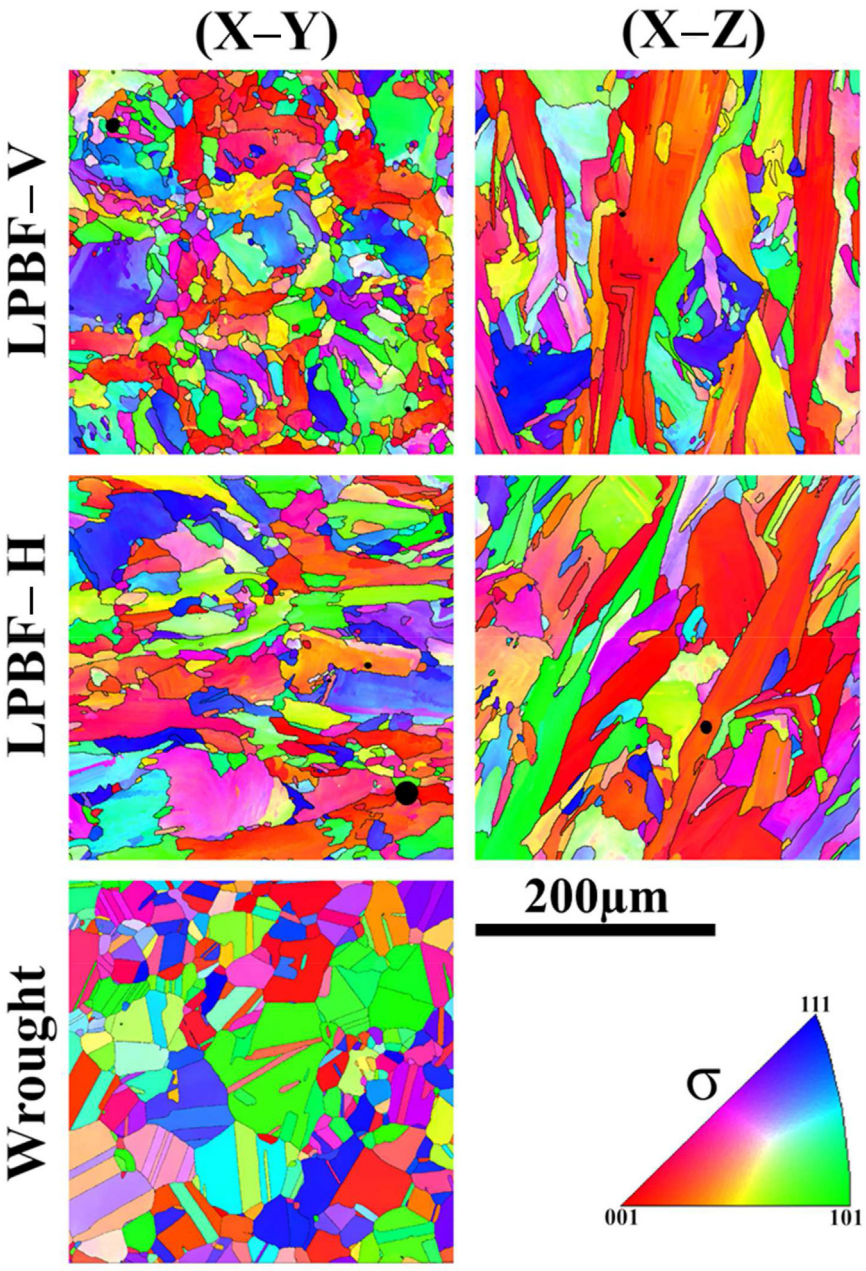

Fig. 4 – Inverse pole figure maps for the LPBF IN718 material in the vertical and horizontal orientations, given in the X–Y and the X–Z planes, in addition to wrought IN718.

3. Results and discussion

3.1. *Material*

The microstructures of the LPBF and wrought IN718 variants are given in Fig. 4, where the inverse pole figure (IPF) maps are shown in the X–Y and X–Z planes for the two LPBF orientations, and the X–Y plane for the wrought material. It can be seen in that there is a small degree of texture present in the LPBF IN718 material in the <100> orientation, and a difference in aspect ratio of the grains is seen between the two reference planes inspected. In the case of the vertically orientated material, the grains are elongated parallel to both the build direction and the stress axis. In each of the respective planes of the LPBF materials, evidence of residual gas porosity from the manufacturing process can be seen. Such features are typical of non hot isostatically pressed (HIP) AM materials, and it is inferred from the sampled area that pores of such dimension are widespread. In contrast, the wrought IN718 area sampled exhibited a far coarser, equiaxed microstructure containing annealing twins and minimal evidence of any process-induced defects.

The grain size characteristics of the IN718 variants are provided in Table 3, presenting the average grain size and aspect ratio values of the different variants as determined by elliptical fitting of the grains reconstructed in EBSD analysis. It is shown that the LPBF IN718 material exhibits a finer grain

Table 3 – Grain size measurements of wrought and LPBF IN718 variants. Standard deviation values are given in italic text.

		Mean Grain size, d (μm)	St Dev	Aspect Ratio	St Dev	Recrystallisation (%)
Wrought		24.4	17.08	1.69	0.62	99.9
LPBF-V	X–Y	11.0	8.07	2.05	0.83	66.6
	X–Z	13.7	12.53	3.35	2.52	71.2
LPBF-H	X–Y	12.6	11.10	2.70	1.54	53.7
	X–Z	15.4	13.19	3.39	1.98	77.9

size than the wrought counterpart, and the grain size distribution shows a smaller spread. A prominent feature is the increased aspect ratio of grains in the LPBF material, particularly in the sampled plane containing the build direction (X–Z). The elliptical fitted grain data presented in terms of the arithmetic mean of the size and aspect ratio is greatly influenced by the presence of small grains in the LPBF materials, which are often present in colonies and are particularly prevalent in the X–Y plane IPF maps given in Fig. 4.

In addition to grain size and aspect ratio, the degree of recrystallisation was also calculated using an area basis and ignoring boundary reconstructed grains. Using this approach, the wrought IN718 material was found to be 99.9% recrystallised. In contrast, the LPBF materials exhibited significantly reduced recrystallisation fractions. Indeed, a large variation in measured values was observed within each orientation when considering the individual sections, as the presence of the build direction in the sampled plane significantly influenced the number of grains sampled, further influenced by disregarding the boundary grains. Recrystallisation fractions were observed to be 71.2% and 77.9% for the vertical and horizontal material in the X–Z plane (parallel to the build direction), which reduced to 66.6% and 53.7% respectively for the X–Y planes, perpendicular to the build direction. It is likely that the presence of the smaller grain colonies and the relatively small sample area contributes to this observation.

Additional microscopy is provided in the form of FEG-SEM imagery to reveal the distribution of secondary strengthening phases such as incoherent interstitial and intermetallic compounds including carbides and δ phase, in both the wrought and LPBF materials. The micrographs in Figs. 5 and 6 present the morphologies and chemical compositions of the microstructural features for the wrought and LPBF vertically built material on the X–Y plane, respectively. Fig. 5 shows a small number of grain boundary carbides in wrought IN718, with Fig. 5b displaying a fine globular dispersion of Nb-rich MC carbides (as indicated by the red crosshair and arrow) forming as discrete particles of approximately 1–3 μm in diameter. Similarly, a small number of grain boundary MC carbides are also located in the LPBF material (Fig. 6), albeit at a slightly smaller scale up to a maximum diameter of approximately 1 μm. The main difference between the two material variants is the significantly greater presence of δ phase at the grain boundaries in the LPBF material, as illustrated by the sharp white features. The δ phase (as indicated by the yellow crosshair and arrow) in the LPBF material is found to be much smaller and is located at both grain boundaries and within grains, as opposed to the wrought material where it appears to be coarser and predominantly transgranular with relatively few intergranular features. The elemental compositions of the features mirror those previously reported by Ferreri et al. [35].

Ni based superalloys are renowned for their high temperature capability, and their strength is primarily attributed to the presence of γ′ and γ″, which are coherent or semi-coherent secondary phases that typically provide the greatest contribution to hardening IN718. The primary compositions of each are $Ni_3(Al,Ti,Nb)$ for γ′ and $Ni_3(Nb,Ti)$ for γ″. The precipitation of both phases occur during heating of the primary face centred cubic (FCC) γ phase, where increased solute mobility allows for localised elemental segregation. However, the γ″ phase is metastable at room temperature and can transform from being a body centred tetragonal (BCT) phase into an orthorhombic δ phase ($Ni_3(Nb,Ti)$) when subjected to elevated temperature for an extended period or exposure to sufficiently high temperatures [36]. Incoherent phases, such as MC carbides and δ phase, can then aid grain size refinement and improve strength based properties if located at grain boundaries, since they will impede grain boundary sliding. However, if they are exceedingly coarse and acicular, they can be detrimental to ductility since they promote reduced dispersion hardening.

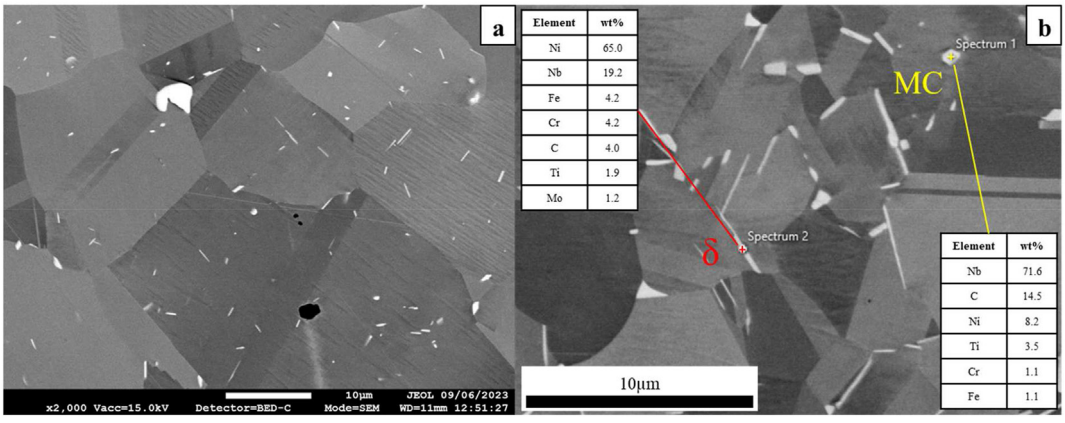

Fig. 5 – a) Micrograph of MC carbides and δ phase formations and b) EDS elemental analysis of MC carbides (yellow crosshair) and δ phase (red crosshair), in wrought IN718 material.

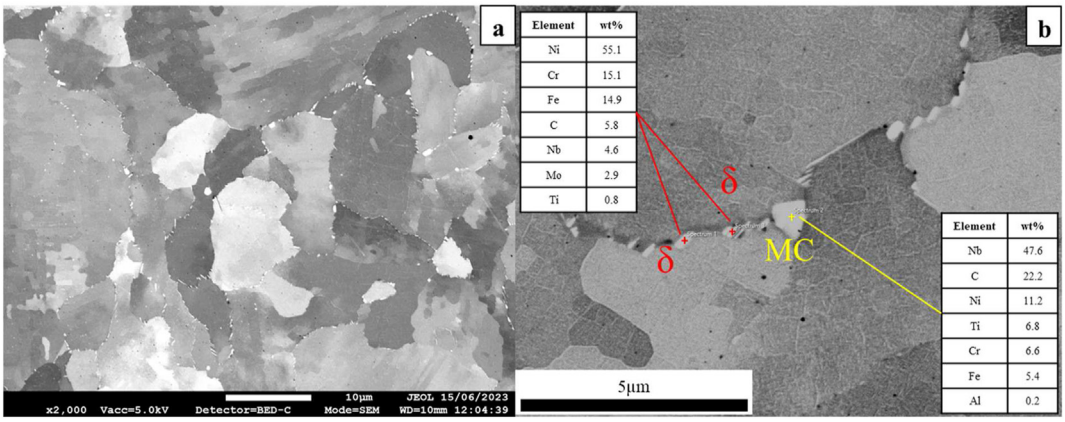

Fig. 6 – a) Micrograph of MC carbides and δ phase formations and b) EDS elemental analysis of MC carbides (yellow crosshair) and δ phase (red crosshairs), in LPBF vertically built IN718 material on the X–Y plane.

3.2. *Mechanical results*

3.2.1. *Uniaxial tensile results vickers hardness (H_v) testing*

The mechanical property data generated from the five uniaxial tensile tests on each variant is displayed in Table 4, along with the standard deviations. The wrought material is significantly outperformed by the LPBF variants in regard to yield and ultimate tensile strength properties, with the horizontally built additive material exhibiting the strongest response, but the wrought variant does offer a far greater ductile performance regarding percentage elongation and reduction in cross-sectional area (RA). The behaviours of these variants are linked to their microstructural morphologies, with the grain sizes of the LPBF material being very similar, and minimal difference is seen across all four material properties. In contrast, the average grain size of the wrought variant is approximately double that of the LPBF samples. As such, the reduced grain boundary area present in the wrought alloy results in a significant reduction in the tensile properties compared to the LPBF samples.

In regards to the presence of secondary strengthening phases, Ferreri et al. [37] previously found that LPBF IN718 had a significantly lesser content of the γ′′ phase as compared to the wrought material, but exhibited a far higher volume fraction of δ phase. This in turn led to a superior tensile response in the LPBF material, achieving a σ_y of approximately 1275 MPa, as compared to the wrought alloy (1115 MPa). This is also true of the current study, with a pronounced presence of grain boundary δ phase in the LPBF material which has subsequently led to a stronger tensile performance. The behaviour of these properties also follows a similar trend to that found by Hosseini et al. [38] who undertook an extensive review of the mechanical response of AM IN718. They found that, in general, horizontally built LPBF IN718 had superior σ_{UTS} and σ_y properties, with reduced ductility, as compared to the vertically built equivalent. Furthermore, the values generated in the current research fell within the ranges that Hosseini defined in their paper, where they considered and compared a series of results from several different sources [38].

3.2.2. *Small punch tensile and shear punch tensile results*

A similar behaviour is seen when observing the ShP response, as shown in Fig. 7a. The two LPBF materials again exhibit far superior maximum strength (τ_{USS}) and proof strength (τ_{PS}) values, yet a far more brittle response in comparison to the wrought material, which offers three times the displacement. This behaviour can be related to the underlying microstructure in the different materials, with the greater strength properties (as listed in Table 5) in the LPBF material attributed to the smaller average grain size compared to the wrought variant.

This is in stark contrast to the material responses from the SP test, as displayed in Fig. 7b and presented in Table 6. Under SP, the wrought material withstands a superior maximum force (F_{MAX}=3005 N) as compared to the LPBF materials (LPBF V = 1618 N and LPBF H = 1706 N), and also the highest level of displacement. It is also important to note here that for SP and ShP testing, the LPBF material was only tested on a single face for each of the build directions, namely the vertically built material on the X–Y plane, and for the horizontally built variant, on the X–Z plane. This is due to the nature in which the disc specimens were sourced. In both instances, SP discs were extracted perpendicularly from the threaded regions of the uniaxial tensile specimens for each respective build

Table 4 – Uniaxial tensile properties of wrought and LPBF IN718 variants. Standard deviation values across the five tests are given in italic text.

Material	E (GPa)		$\sigma_{PS0.2}$ (MPa)		σ_{UTS} (MPa)		Elongation (%)		RA (%)	
Wrought	173	*8.39*	561	*3.03*	986	*6.18*	37.5	*1.09*	42.8	*2.06*
LPBF V	193	*8.25*	1286	*25.03*	1434	*7.56*	19.6	*0.48*	35.0	*1.78*
LPBF H	196	*6.46*	1311	*3.85*	1507	*3.24*	18.0	*1*	28.0	*0.71*

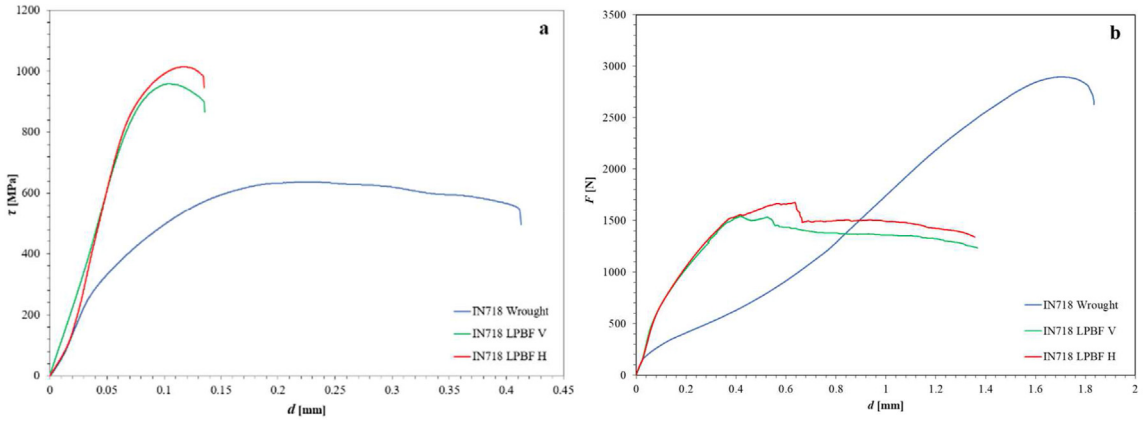

Fig. 7 – Indicative mechanical response of the wrought and LPBF IN718 variants under a) ShP loading and b) SP loading.

orientation. Given the cylindrical geometry of the samples, it was not deemed feasible to extract discs in the orthogonal direction.

Despite these differences, correlations to uniaxial properties can be made through empirical relationships, based on the average results generated under each test type, as displayed in Tables 5 and 6 SP yield force, or F_e, as determined through the bilinear, two-tangents method, can be correlated to yield strength (σ_y) through the relationship defined in Eq. (2). For ShP, the yield strength value is calculated via an offset shear yield stress (τ_{PS}) which as discussed previously is defined as the intersecting point between the τ - d/t curve and a force offset line parallel to the linear portion. Further detail on this is given in [15]. This value can then be correlated to σ_y through the relationship given in Eq. (3) (for ShP):

$$\sigma_y = \alpha_1\left(\frac{F_e}{t^2}\right) + \alpha_2 \tag{2}$$

$$\sigma_{PS} = m_1\tau_{PS} + n_1 \tag{3}$$

where α_1 and α_2 are SP constants and m_1 and n_1 are ShP constants calculated from linear regression from a series of results, and t is the original thickness of the disc specimen at the start of the test. This equation can also be modified in order to define uniaxial proof stress, σ_{PS}, for a SP test using the same values. Likewise, an estimation of σ_{UTS} values from the F_{MAX} and τ_{USS} values generated in a SP (Eq. (4)) and ShP (Eq. (5)) test can also be determined through the following relationships:

$$\sigma_{UTS} = \beta_1\left(\frac{F_{MAX}}{t\cdot d_m}\right) + \beta_2 \tag{4}$$

$$\sigma_{UTS} = m_2\tau_{USS} + n_2 \tag{5}$$

where β_1 and β_2 are SP constants and m_2 and n_2 are ShP constants derived from linear regression. It is important to note here that for the correlations relating to SP loading conditions, an additional factor, d_m, is also employed. d_m relates to the deflection at the point of F_{MAX} and is included since under SP loading, the disc specimen deforms under a complex and evolving biaxial stress field. This additional parameter ensures that the level of displacement observed is appropriately accounted for. Finally, to estimate elongation, El, values from the deflection at F_{MAX} and τ_{USS} (d_m) can be used, according to the following two relationships, for SP (Eq. (6)) and ShP (Eq. (7)) respectively:

$$El = \gamma_1\cdot d_m \tag{6}$$

$$El = m_3 d_m \tag{7}$$

where γ_1 and m_3 are SP and ShP constants, respectively.

Table 5 – Shear punch tensile properties of wrought and LPBF IN718 variants. Standard deviation values across the five tests are given in italic text.

Material	τ_{USS} (MPa)		τ_{PS} (MPa)		$d@F_{MAX}$ (mm)	
Wrought	648	*15.83*	268	*5.03*	0.23	*0.02*
LPBF V	934	*25.48*	760	*1.64*	0.11	*0.01*
LPBF H	1001	*17.58*	732	*4.86*	0.12	*0.06*

Typically, the constants used in Eqs. (2)–(7) are determined using a range of material data sets, however, since the results in this study are across only three variants, the constants have been adopted from a previous study by the same authors [15]. Lancaster et al. undertook a similar study on a far more encompassing range of metallic materials and were able to derive constants across a collection of materials with varying properties, achieving sufficiently high R^2 values ($R^2 > 0.93$) for strength based parameters. Using these constants, reproduced and displayed in Table 7, predicted uniaxial properties from ShP and SP results were calculated; these values are displayed in Table 8.

As can be seen, the predicted values have shown a good level of agreement with the uniaxial properties, particularly in regard to σ_{UTS}, $\sigma_{PS0.2}$ and El for ShP, and σ_{UTS} and σ_y for SP. When comparing the predicted σ_{UTS} from ShP and SP results, the maximum percentage variation as compared to the uniaxial properties stated in Table 4 are 13.9% (for ShP) and 19.8% (for SP) across the three material types, respectively. ShP testing was also found to follow the same ordering seen in the uniaxial properties, where the wrought material exhibits the lowest predicted σ_{UTS} value (873.8 MPa), followed by the

Table 6 – Small punch tensile properties of wrought and LPBF IN718 variants. Standard deviation values across the five tests are given in italic text.

Material	F_{MAX} (N)		F_e (N)		$d@F_{MAX}$ (mm)	
Wrought	3005	*76.41*	237	*50.67*	1.72	*0.01*
LPBF V	1618	*47.64*	640	*90.44*	0.50	*0.06*
LPBF H	1706	*30.5*	621	*20.10*	0.66	*0.04*

vertically built LPBF material (1234.4 MPa), and finally the horizontal LPBF orientation which offers the strongest response (1319.5 MPa). This contrasts with the behaviour seen in the SP based calculations. Whilst the wrought material is again significantly weaker (846.6 MPa) compared to the LPBF variants, the vertically built specimens show the strongest predicted response (1504.8 MPa), far exceeding the predicted σ_{UTS} value of the horizontal samples (1214 MPa). This change in ordering can be related to two main factors. Firstly, it is important to consider that the constants used in this research were adopted from a previous study on homogeneous, wrought based materials that typically exhibit minimal evidence of anisotropy. Here, as given in the EBSD inverse pole figure maps presented in Fig. 4, the LPBF material shows a level of anisotropy on the alternative X–Y to X–Z faces, as commonly seen in AM based structures. Secondly, the biaxial manner of deformation attributed to SP testing needs to be acknowledged. As given in Fig. 4, when a horizontally orientated disc specimen is subjected to SP loading, the X–Z plane is the face that is biaxially deformed through the test. Likewise, when the vertical disc is tested under SP conditions, the face being deformed is the X–Y plane. As such, it may be more appropriate to correlate the uniaxial properties of the vertical LPBF material with those generated in the X–Z plane, i.e. the material nominally recognised as 'horizontal'. In doing so, the ranking of the predicted σ_{UTS} resumes the same ordering as that seen in uniaxial testing. This also improves the percentage variance, where the X–Y plane (otherwise known as the 'vertically' orientated material) has a variance of only 0.14% compared to the horizontal LPBF material under uniaxial conditions (predicted = 1504.8 MPa, actual = 1507 MPa). A similar approach was also adopted when correlating the uniaxial and SP derived properties on LPBF C263 [10].

A similarly inverted behaviour is seen when analysing the predicted σ_y properties for SP testing as compared to the uniaxial values, where the calculations for the vertically orientated LPBF material offers a slighter stronger response as compared to the horizontal equivalent. However, if the values are changed so that the disc taken from X–Z plane i.e., the horizontally built material, is compared against the vertical uniaxial properties, the percentage variation widens. It should be noted here that care must be taken, since the difference in predicted σ_y properties for the vertical and horizontally built samples is reasonably small (1031 MPa for vertical, 1000 MPa for horizontal), and this could simply be attributed to be within the band of material scatter (approximately 3%). This is also the case for the predicted percentage elongation values. SP has successfully been able to recognise the considerable ductility observed in the wrought material as compared to the LPBF based samples (35.2% for wrought, 10.1% for LPBF V and 13.4% for LPBF H) and changing the properties to be able to correlate the actual tested microstructure more accurately, results in a widening of the variation percentage. Yet, the difference between the two values is not considerable enough so that scatter should not be factored in, plus, the level of standard deviation, particularly for the LPBF V material, is of a reasonable value to highlight that scatter should be considered.

A similar consideration under ShP conditions is not believed to be necessary, since the deformation mode is through shear in the Z-direction through the material (as shown previously in [15]), more closely replicating the behaviour observed in uniaxial deformation, in regard to the principal material orientations that are actually being deformed in a ShP and uniaxial tensile test. In addition to this, when considering the three properties that have been compared (namely σ_{UTS}, $\sigma_{PS0.2}$, and *El*), there is far less directional difference in the predicted properties between vertical and horizontal built samples, as compared to the same properties when calculated from SP results. Upon reflecting on the uniaxial generated properties, there is only 26 MPa difference in σ_{UTS}, 73 MPa difference in $\sigma_{PS0.2}$, and 0.8% difference in elongation. This compares favourably with the difference seen in the predicted uniaxial properties from ShP data (85 MPa difference in σ_{UTS}, 51 MPa difference in $\sigma_{PS0.2}$, and 1.2% difference in elongation). Therefore, ShP testing has been shown to be an effective method of determining the subtle differences that exists between LPBF build orientations for all three tensile based properties.

Table 7 – Constants used for correlations of SP and ShP data to uniaxial properties, taken from [15].

Test Type	Parameter									
	m_1	n_1	m_2	n_2	m_3	α_1	α_2	β_1	β_2	γ_1
Shear Punch	1.39	59.4	1.26	56.67	166.11					
Small Punch						349.1	133.48	0.22	89.74	20.42

3.2.3. *Profilometry-based indentation plastometry (PIP) results*

A series of single PIP indents were collected on each of the planes of the wrought and LPBF IN718 variants. Fig. 8 shows the tensile stress-strain curves for the different alloy variants generated from PIP testing, up to the point where the σ_{UTS} is reached. As can be seen, there are three distinctly different behaviours observed across the materials. Similar to the behaviours observed under uniaxial tensile, SP and ShP testing, PIP has clearly detected the anisotropy present in the LPBF IN718 samples, both of which significantly outperform the strength based properties of the wrought material. Whereas the wrought variant achieved a σ_y value of 530 MPa, the two faces of the horizontally built LPBF material yielded at 1338 MPa (X–Y) and 1360 MPa (X–Z), whilst the vertical material reached 1622 MPa (X–Z) and 1649 MPa (X–Y), more than three times that found in the wrought alloy. In terms of the σ_{UTS} values, wrought IN718 achieved 968 MPa, LPBF H reached 1512–1555 MPa and LPBF V reached 1622–1655 MPa. For the wrought material, these values are in good agreement with

Table 8 – Predicted uniaxial tensile properties from ShP and SP results. The percentage variance (Var.) between the measured uniaxial properties (taken from Table 4) and predicted results is also provided.

Material	Shear Punch predicted properties						Small Punch predicted properties					
	σ_{UTS} (MPa)	Var. (%)	$\sigma_{PS0.2}$ (MPa)	Var. (%)	*El. (%)*	Var. (%)	σ_{UTS} (MPa)	Var. (%)	σ_y (MPa)	Var. (%)	*El. (%)*	Var. (%)
Wrought	873.8	11.4	432.7	22.8	38.5	2.7	846.6	14.2	463.9	17.3	35.2	6.2
LPBF V	1234.4	13.9	1116.2	13.2	18.5	1.8	1504.8	5.0	1030.8	19.8	10.1	46.1
LPBF H	1319.5	12.4	1065.4	18.8	19.7	9.6	1214.4	19.4	1000.4	23.7	13.4	25.4

the properties generated from uniaxial tensile testing, whereby the differences between yield and ultimate tensile strength values are 31 MPa (for σ_y) and 28 MPa (for σ_{UTS}), which is less than 6% across both properties. Likewise, there was minimal difference between the two contrasting data sets when considering the LPBF horizontal variants, with only 2% (X–Y) and 3.5% (X–Z) difference for σ_y, and less than 1% (X–Y) and 3.5% (X–Z) deviation for σ_{UTS}.

For the LPBF IN718 material sectioned from vertically built specimens, there was no significant difference in the σ_{UTS} and σ_y values of the specimens, regardless of orientation, predicting near perfectly elastic-perfectly plastic behaviour up until the σ_{UTS} is reached, which was found to be achieved at approximately 2% strain; where typical yield/tensile values of 1622 MPa and 1649 MPa were achieved for the LPBF-V X–Y and X–Z faces, respectively. The nature of the stress-strain curve that was generated is inconsistent with the other material variants, with σ_{UTS} being reached after a far smaller level of strain (11.5–14% for LPBF H, and 19% for wrought). It is unclear as to why this behaviour has occurred in only the vertically built LPBF sample, and there is currently little previous literature that explains such issues given the uniqueness of the technique and the ongoing development of understanding of the test method. In previous research, Tang et al. [20] adopted PIP testing to characterise the tensile properties of the age-hardenable nickel based superalloy, ABD-850AM, manufactured via LPBF. Since the alloy was produced via LPBF, the microstructure exhibited a level of anisotropy and crystallographic texture, as is typical from the LPBF process. However, Tang et al. also stated that since indentation effectively deforms a material in multiple directions, the end result is likely to be an average of a multi-directional deformation field. For an isotopic material, this would not be expected to be an issue, as was found here in the wrought alloy where only a 6% difference was found between the uniaxial tensile and PIP generated strength based properties. Yet, for strongly anisotropic materials, as is usually the case in LPBF materials, a more complex modelling procedure is required that contains additional parameters to account for such directionality. Given these issues, the values generated through PIP testing do not compare as favourably to the uniaxial properties as was found for the horizontally built and wrought equivalents, where percentage differences of 21% (X–Z) and 22% (X–Y) were found for σ_y, and 12% (X–Z) and 13.5% (X–Y) for σ_{UTS}. Despite these discrepancies, there is still a reasonable agreement between the uniaxial and PIP generated properties and the test technique could be used for testing anisotropy between different build orientations, and to obtain a semi-quantitative measure of a materials' strength based properties. Although, there is a concern in the changing of the ordering of the different variants. Whereas in uniaxial tensile, SP and ShP testing, the wrought material was clearly the weakest, followed by the vertically built LPBF alloy with the horizontal equivalent performing the strongest, for PIP that

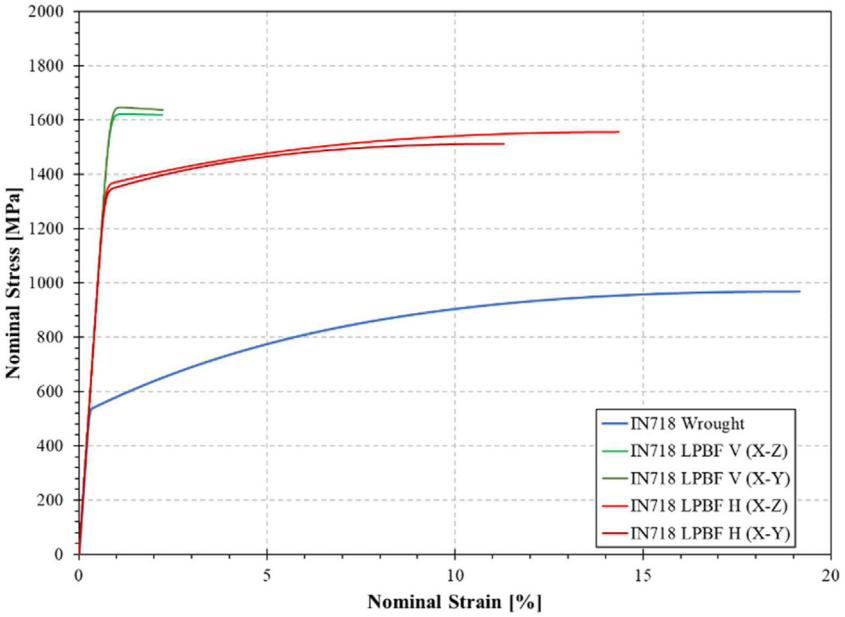

Fig. 8 – Simulated nominal stress versus nominal strain curves for wrought and LPBF IN718 variants generated via PIP.

ordering changes, with the vertical LPBF material outperforming the horizontally built variant. This could be attributed to the difference in the deformation behaviour across the different test methods. When a material is tested under uniaxial, SP or ShP conditions, the specimen is loaded until failure occurs in the form of a fracture. However, for PIP testing, the deformation is more akin to hardness and nanoindentation, where a load is applied to the specimen surface through an indentation tooling. Measurements of the indentation morphology are then taken, from which properties can be calculated. It is important to consider that the algorithms used in PIP testing to derive a stress-strain curve from the indentation loading and resulting morphology account for true stress-true strain behaviour. In previous research, Tang et al. [20] saw a similar behaviour when performing uniaxial tensile and PIP testing on LPBF ABD-850AM built in the vertical and horizontal orientations, where they found that the horizontally built material exhibited superior strength based properties under uniaxial tensile loading, but the vertical material was stronger under PIP. The authors continued that the vertical material experienced a greater reduction in cross-sectional area upon fracture, as was also the case here (see Table 4), and if true stress-true strain conditions were employed to predict fracture, then it would be expected that this value would be higher for the vertical sample. This same principle applies as stated in previous research of LPBF IN718 [39] and is shown more explicitly in a related study on wire and arc additively manufactured (WAAM) IN718 which has a similar overall microstructural formation, i.e., epitaxial grain growth, to that seen in LPBF IN718 [40].

3.2.4. *Vickers hardness (H_v) and nanoindentation results*

Fig. 9 presents the results from the hardness testing. The results show again that the wrought material has the weakest response, followed by the LPBF horizontal and vertical materials, which behave very similarly. Interestingly, like the PIP based results, the vertical LPBF material slightly outperforms the horizontal equivalent (by 5 H_v on the X–Z plane, and 4 H_v on the X–Y plane, both of which exhibit less than 1% difference), and this can be linked to the grain size measurements seen across the different planes. Whereas the vertical material has an average grain size on the X–Z plane of 11.0 μm and X–Y plane of 13.7 μm, the horizontally built variant has measurements of a similar order (15.4 μm on the X–Z plane and 12.6 μm on the X–Y), albeit being slightly coarser. This is reflected in the result where the vertically built material is found to be slightly harder than the horizontal variant and this can be linked to the renowned Hall-Petch theory.

Historically, hardness values have been used to approximate uniaxial tensile σ_{UTS} values through the following expression [41,42]:

$$H_v = 3\,\sigma_{UTS} \tag{8}$$

Based on this approximation, the predicted σ_{UTS} for the wrought material is 1061 MPa (as opposed to 986 MPa from the uniaxial tensile testing), 1458–1476 MPa for the vertically built LPBF material (compared to 1434 MPa) and 1448–1462 MPa for the horizontal LPBF material (compared to 1507 MPa from the actual tests). Therefore, H_v can be considered as a suitable semi-quantitative means of obtaining an approximation of σ_{UTS} for all three IN718 variants, with a maximum deviation of 7%. Caution must be taken however, since this empirical relationship has limited validity for materials that work harden. For work hardening metals, Tabor [43] suggested that the yield strength/ultimate tensile strength should be replaced by the uniaxial flow stress at a specified value of strain. For a Vickers hardness indenter, this strain would be approximately between 8% and 10%, and the hardness value would then be 3 times the flow stress at this specific strain.

Hardness measurements were also recorded on a smaller scale through nanoindentation. Fig. 10 presents the average hardness values determined from 4 x 4 arrays of

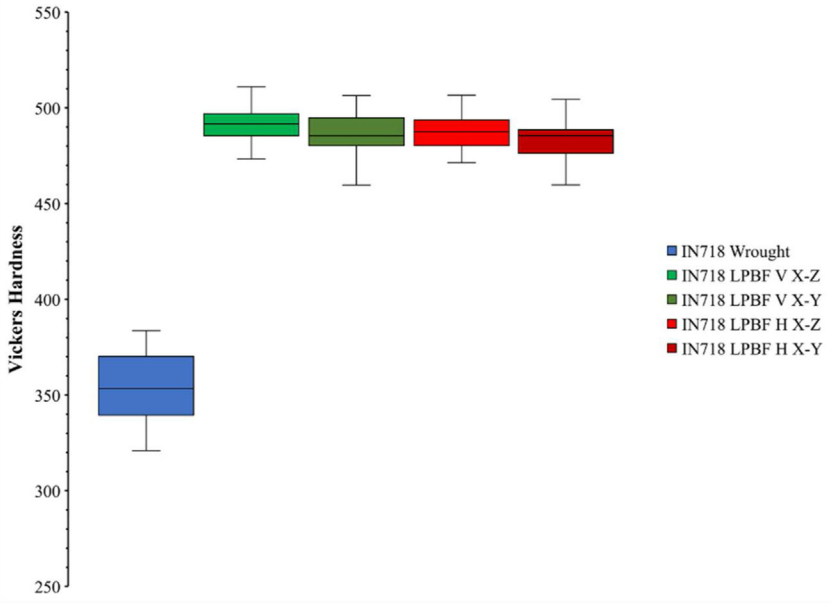

Fig. 9 – Vickers hardness (H_v) response of wrought and LPBF IN718 variants.

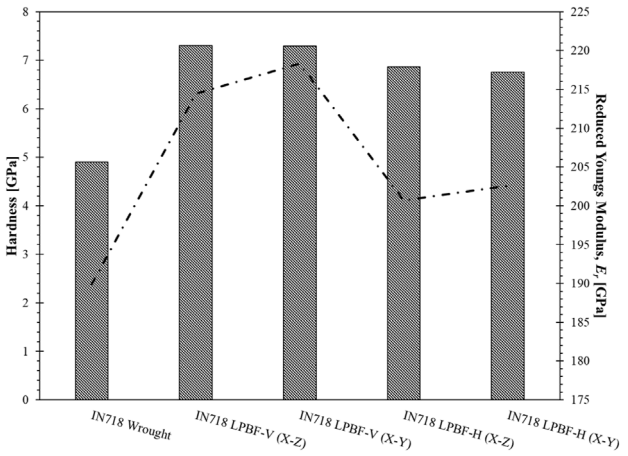

Fig. 10 – Hardness and reduced modulus properties determined via nanoindentation for wrought and LPBF IN718 variants.

nanoindentations in each plane for each of the IN718 specimen variants. The results are in good agreement with the micro-scale Vickers hardness testing performed in terms of an increase in hardness from wrought material to that produced by LPBF and also the relative hardness of the LPBF material in each orientation and reference plane. Previously, a scalar function of 9.807 was derived when attempting to convert between Hv and GPa from micro- and nano-hardness based experimentation [44]. Using such an approach provided values of 3.47 GPa, 4.83 GPa, 4.77 GPa, 4.78 GPa and 4.73 GPa for wrought, LPBF V X–Z, LPBF V X–Y, LPBF H X–Z and LPBF X–Y respectively. These predicted values are in reasonable agreement to the hardness values generated through nanoindentation, where values of 4.9 GPa, 7.3 GPa, 7.3 GPa, 6.85 GPa and 6.75 GPa were generated for the respective variants and orientations. However, it is important to consider other factors that can play a key role across different length scales. It is undetermined whether the differences between the predicted and experimental values relate to a broad surface effect or, and perhaps more likely, the increased influence of secondary phases such as precipitates, MC carbides and δ phase, particularly in the LPBF variants (See Figs. 5 and 6). These effects are likely to be less influential under microhardness conditions where grain size acts as the key contributor to the mechanical response, but can clearly have a greater impact under nanoindentation conditions due to the scale of the indentation.

The reduced Young's modulus determined during the unloading phase, is also displayed in Fig. 10. Similar to the behaviours observed under uniaxial tensile loading, a consistently higher reduced modulus is obtained in the LPBF samples as compared to the wrought material, with the vertical LPBF variant exhibiting the highest values (215–218 GPa), followed by the LPBF horizontal material (201–203 GPa) and the wrought alloy exhibiting a reduced modulus approximately 13% less than the highest value (190 GPa). This is a similar percentage difference (12%) to that seen under uniaxial testing conditions, where the best performing LPBF material achieved a Young's modulus of 196 GPa and the wrought material 173 GPa. It has previously been reported [45] that the reduced modulus (E^*) can be related to the Young's modulus (E) through the following equation:

$$E^* = \frac{E}{(1-\upsilon^2)} \tag{9}$$

Where υ relates to the material's Poisson's ratio, which for IN718 is taken as 0.29 from a previous study [24]. Using this equation, the predicted Young's modulus for the wrought material has excellent agreement with the experimentally derived value (174 compared to 173 GPa). However, for the LPBF materials, the relationship is less clear. For the vertical LPBF variant, the predicted values are 197 GPa (X–Z) and 200 GPa (X–Y), which are a slight over prediction of the experimental value (193 GPa) by 2 and 3.5% respectively, whilst for the horizontally built material, the predicted values underpredict the actual response, providing values of 184 GPa (X–Z) and 186 GPa (X–Y), as opposed to 196 GPa from the uniaxial tensile testing (by 6% and 5% respectively). The first factor to consider here is the changing of ordering of the modulus values. As seen in PIP and H_v, the vertical LPBF variant offers the superior properties followed by the horizontal equivalent. Yet under uniaxial, SP and ShP loading, the ordering changes whereby the horizontal material offers a stronger performance across all three strength related properties (E, $\sigma_{PS0.2}$, σ_{UTS}).

As seen in the H_v results, while the hardness performance of each respective material variant can be explained in part by the underlying grain size, for nanoindentation, the indentation size is much smaller than a single grain, thus indicating that an additional factor is also having an influence. Wang et al. [24] previously looked at the nanoindentation based properties of AM IN718 and attributed the difference in nanohardness to the presence of geometrically necessary dislocations (GND) in the AM material. GNDs are effective at inhibiting slip, thus improving yield strength and hardness. Furthermore, it is possible that pile up/storage of GND's can inhibit slip further, leading to additional strengthening. As given in Fig. 11, it appears that pile up is quite pronounced in both the wrought and LPBF materials investigated in this study, with a greater extent of pile up occurring in the wrought variant. This would suggest that the LPBF material exhibits a stronger resistance to slip, and therefore, a superior performance. Likewise, the pile up height in the vertical LPBF material is marginally less than the horizontal equivalent, indicating a similar ranking of the materials as found under PIP and H_v testing. Wang et al. [24] continued that since the full effect of GNDs may be related to the orientation of slip systems, they may also contribute a small amount to the anisotropy seen in the results. They found that the hardening effect for their AM material is more pronounced for the Vickers microhardness (~12%), which may be attributed to the combination of the Hall-Petch and GND effects.

In a similar study to understand the role of microstructure on pile up formation, Rifat et al. [25] performed a series of nano-scratches on LPBF IN718 using a spheroconical diamond indenter. In this research, the authors compared the as-received LPBF material to samples that had undergone a homogenising and solution heat treatment. They found that the as-received material experienced a positive correlation

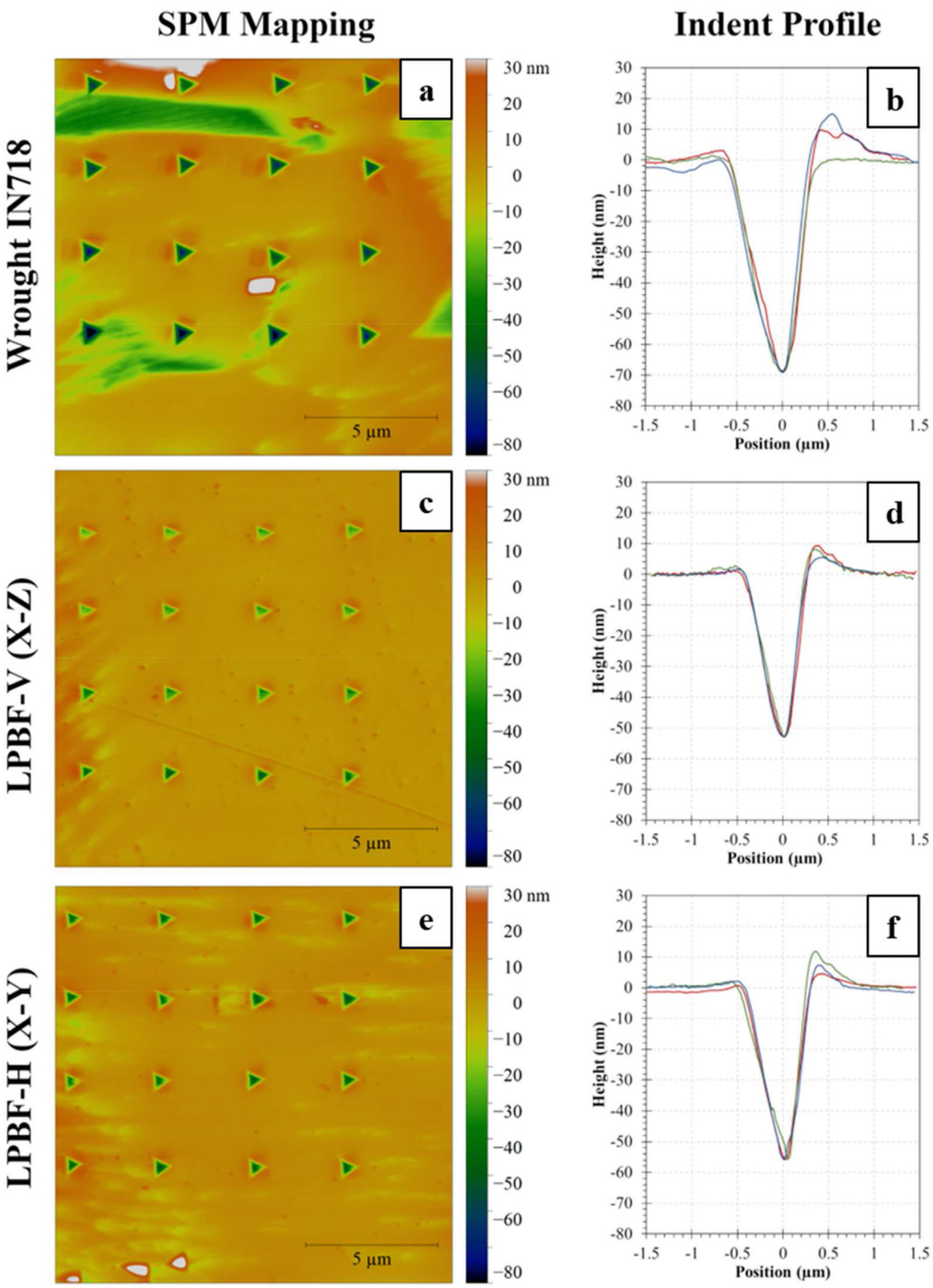

Fig. 11 – a), c), e) Image of nanoindentations and, b), d), f) profile of nano-indents for wrought, LPBF vertical (X–Z) and LPBF horizontal (X–Y) IN718 variants.

between pile up height and scratch depth, whilst for the heat treated material, there was a negative correlation between the two measures, suggesting a transition in the deformation mechanisms. Generally, a positive correlation across pile-up heights and scratch depths implies that a deeper scratch produced a taller pileup, wherein the extra material displaced during the scratch reappeared at the free surface. However, a negative correlation implies that a deeper scratch produced a

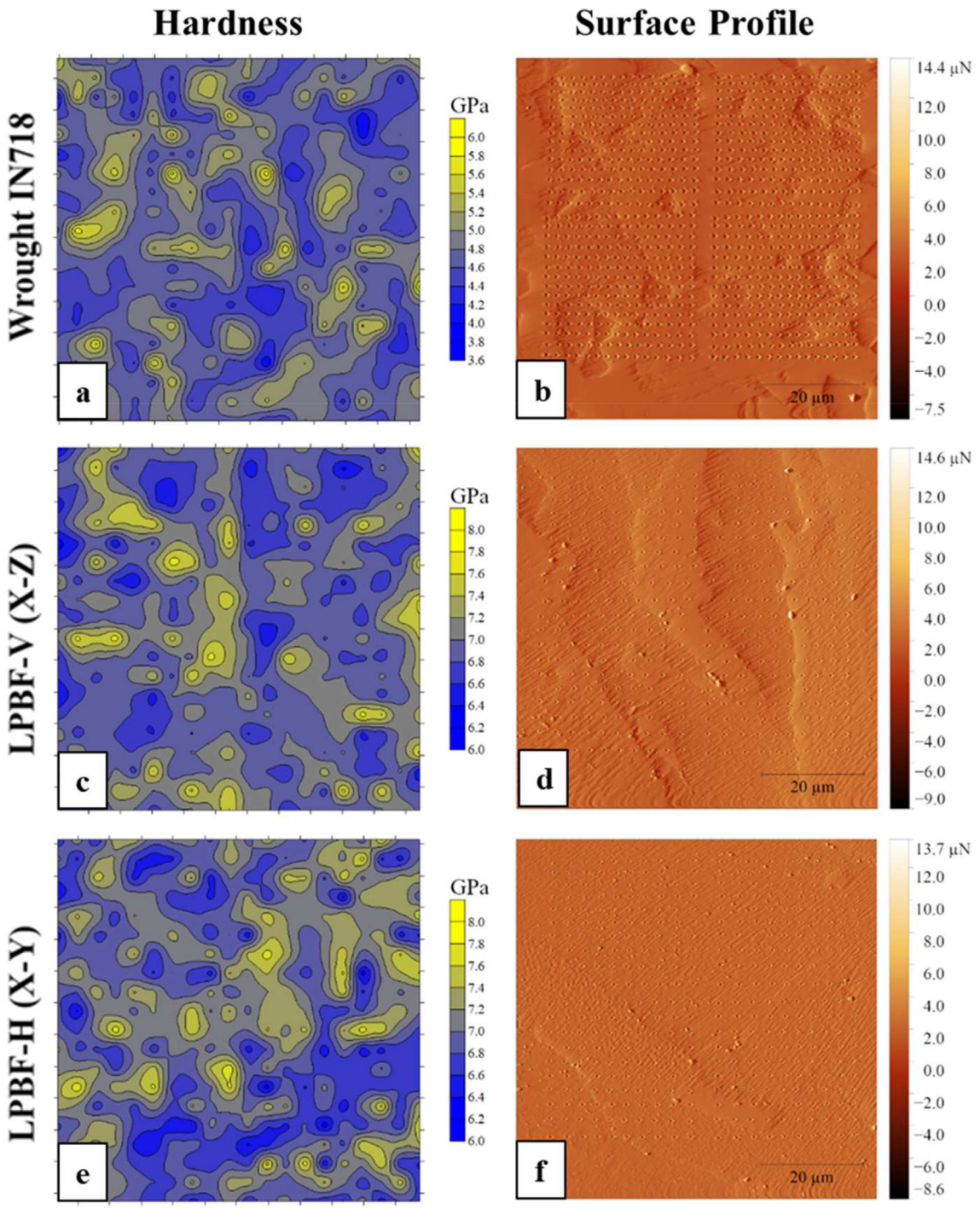

Fig. 12 – a), c), e) Constructed hardness maps from accelerated property mapping (XPM) and, b), d), f) scanning probe microscopy (SPM) for wrought, LPBF vertical (X–Z) and LPBF horizontal (X–Y) IN718 variants.

shorter pileup, wherein the extra material engaged by the deeper scratch was displaced, which has occurred in the LPBF material investigated in this study. Likewise, the superior nanohardness properties of the LPBF materials as compared to the wrought equivalent could be due to microplastic phenomena aided by the greater presence of the δ phase at the grain boundaries (see Fig. 6). The δ phase can produce sharper deformation gradients under the action of the indentation which then lifts up under the action of the consistent normal force. Such behaviour can be seen in Fig. 11 when comparing the profile of the wrought material to the LPBF samples, where a slightly sharper gradient, with a reduced amount of pile up, can be seen in the LPBF material. Rifat et al. [25] also experienced a similar difference between the as-built and heat treated LPBF variants of IN718, where the heat treated sample exhibited a sharper deformation gradient under nano-scratching. They found that the secondary phases in the heat treated specimen were effective at trapping dislocations

before they were able to reach the surface to produce pile ups. The authors also linked the presence of the secondary phases in producing a marginally larger valley roughness, which likely resulted in a larger resistance to scratching.

In addition to individual indents, accelerated property mapping (XPM) was undertaken where 4 concatenated 10 x 10 arrays were analysed for each material/plane. Hardness maps were constructed using a 1000 x 1000 regular grid and Kriging interpolation to examine spatial variance. In each case, measured values outside 2σ were discarded to reduce the influence of anomalies associated with accelerated testing; this was typically 10–12 results. The resulting hardness maps for wrought IN718, vertical LPBF IN718 (X–Z) and horizontal LPBF IN718 (X–Y) are given in Fig. 12. Also shown in Fig. 12 is the associated force maps generated during post-indentation scanning probe microscopy (SPM), indicating the location of the indentations relative to grain boundaries and precipitates present at the surface. In the wrought material, as depicted in Fig. 12a and b, the hardness can be seen to be distributed following the grain structure present, where a small amount of relief profile has been introduced during the polishing procedure. In the LPBF samples shown in Fig. 12c–f, in addition to the underlying elongated microstructure present on the X–Z plane, an apparent influence of secondary phases in close proximity to the indentations is evident. However, it is not clear whether small grains, or colonies thereof, are present in the sampling taken for the LPBF IN718 and whether the hardness maps are influenced by such features. Nevertheless, nanoindentation offers the spatial resolution to determine material properties across microstructural features, e.g. grain boundaries and contained precipitates, that would not be possible in the other test techniques discussed here.

4. Conclusions

The research presented in this paper has examined the suitability of several mechanical test methods in determining the mechanical properties of additively manufactured IN718, and discussed how the contrasting data sets relate to the more recognised uniaxial tensile properties. From this research, the following conclusions can be drawn:

- The microstructure of the LPBF material exhibited the typical anisotropy and directionality associated with AM, where elongated columnar grain growth was found parallel to the build direction. In contrast, the wrought material exhibited a more isotropic, yet coarser, equiaxed morphology.
- The performance of the IN718 variants under uniaxial, small punch and shear punch tensile testing were found to be predominantly influenced by grain size, and all three test methods exhibited the same ordering of the strength based properties in the three materials (LPBF H > LPBF V > wrought).
- Under Vicker hardness and nanoindentation, the ordering changed (LPBF V > LPBF H > wrought), as secondary strengthening phases were considered to play a more significant role. This was attributed to the presence of δ phase in the LPBF material, which was found to be much smaller in scale and located at both grain boundaries and within grains, as opposed to the wrought material where it was coarser and predominantly transgranular.
- Whereas all five test methods have been shown to be effective in generating results that can be correlated to uniaxial properties, the transition in behaviours has been linked to the nature of the test arrangements. Empirical equations have been shown to be effective in predicting uniaxial properties from SP and ShP data. However, results from profilometry-based indentation plastometry, Vickers hardness and nanoindentation require further interpretation relating to the role of the true stress-true strain behaviour and pile up height before a conclusive trend can be derived.

Data availability

The raw/processed data required to reproduce these findings cannot be shared at this time as the data also forms part of an ongoing study.

Declaration of Competing Interest

The authors declare that they have no known competing financial interests or personal relationships that could have appeared to influence the work reported in this paper.

Acknowledgements

The authors would like to acknowledge the assistance provided by Swansea University's Faculty of Science & Engineering Advanced Imaging of Materials (AIM) Facility, which was funded in part by the EPSRC (EP/M028267/1), The European Regional Development Fund through the Welsh Government (80708) and the Ser Solar project via the Welsh Government.

REFERENCES

[1] Blakey-Milner B, Gradl P, Snedden G, Brooks M, Pitot J, Lopez E, et al. Metal additive manufacturing in aerospace: a review. Mater Des Nov. 2021;209:110008. https://doi.org/10.1016/j.matdes.2021.110008.
[2] Muhammad MS, Kerbache L, Elomri A. Potential of additive manufacturing for upstream automotive supply chains. Supply Chain Forum Int J Jan. 2022;23(1):1–19. https://doi.org/10.1080/16258312.2021.1973872.
[3] Kumar R, Kumar M, Chohan JS. The role of additive manufacturing for biomedical applications: a critical review. J Manuf Process Apr. 2021;64:828–50. https://doi.org/10.1016/j.jmapro.2021.02.022.
[4] Eftink BP, Vega DA, El Atwani O, Sprouster DJ, Yoo YSJ, Steckley TS, et al. Tensile properties and microstructure of additively manufactured Grade 91 steel for nuclear applications. J Nucl Mater Feb. 2021;544:152723. https://doi.org/10.1016/j.jnucmat.2020.152723.
[5] Klahn C, Leutenecker B, Meboldt M. Design for additive manufacturing – supporting the substitution of components

in series products. Procedia CIRP 2014;21:138–43. https://doi.org/10.1016/j.procir.2014.03.145.
[6] Leino M, Pekkarinen J, Soukka R. The role of laser additive manufacturing methods of metals in repair, refurbishment and remanufacturing – enabling circular economy. Phys Procedia 2016;83:752–60. https://doi.org/10.1016/j.phpro.2016.08.077.
[7] Lewandowski JJ, Seifi M. Metal additive manufacturing: a review of mechanical properties. Annu Rev Mater Res Jul. 2016;46(1):151–86. https://doi.org/10.1146/annurev-matsci-070115-032024.
[8] Altıparmak SC, Yardley VA, Shi Z, Lin J. Challenges in additive manufacturing of high-strength aluminium alloys and current developments in hybrid additive manufacturing. International Journal of Lightweight Materials and Manufacture Jun. 2021;4(2):246–61. https://doi.org/10.1016/j.ijlmm.2020.12.004.
[9] Hilal H, Lancaster R, Jeffs S, Boswell J, Stapleton D, Baxter G. The influence of process parameters and build orientation on the creep behaviour of a laser powder bed fused Ni-based superalloy for aerospace applications. Materials Apr. 2019;12(9):1390. https://doi.org/10.3390/ma12091390.
[10] Davies S, Jeffs S, Lancaster R, Baxter G. High temperature deformation mechanisms in a DLD nickel superalloy. Materials Apr. 2017;10(5):457. https://doi.org/10.3390/ma10050457.
[11] Fernández M, Rodríguez C, Belzunce FJ, García TE. Use of small punch test to estimate the mechanical properties of sintered products and application to synchronizer hubs. Met Powder Rep Sep. 2017;72(5):355–60. https://doi.org/10.1016/j.mprp.2016.02.056.
[12] Altstadt E, Ge HE, Kuksenko V, Serrano M, Houska M, Lasan M, et al. Critical evaluation of the small punch test as a screening procedure for mechanical properties. J Nucl Mater Apr. 2016;472:186–95. https://doi.org/10.1016/j.jnucmat.2015.07.029.
[13] Altstadt E, Houska M, Simonovski I, Bruchhausen M, Holmström S, Lacalle R. On the estimation of ultimate tensile stress from small punch testing. Int J Mech Sci Feb. 2018;136:85–93. https://doi.org/10.1016/j.ijmecsci.2017.12.016.
[14] García TE, Rodríguez C, Belzunce FJ, Suárez C. Estimation of the mechanical properties of metallic materials by means of the small punch test. J Alloys Compd Jan. 2014;582:708–17. https://doi.org/10.1016/j.jallcom.2013.08.009.
[15] Lancaster RJ, Jeffs SP, Haigh BJ, Barnard NC. Derivation of material properties using small punch and shear punch test methods. Mater Des Mar. 2022;215:110473. https://doi.org/10.1016/j.matdes.2022.110473.
[16] Hankin GL, Toloczko MB, Johnson KI, Khaleel MA, Hamilton ML, Garner FA, et al. An investigation into the origin and nature of the slope and x-axis intercept of the shear punch-tensile yield strength correlation using finite element analysis. In: Hamilton M, Kumar A, Rosinki S, Grossbeck M, editors. Effects of radiation on materials: 19th international symposium. West Conshohocken, PA: ASTM; 2000. p. 1018–28.
[17] Guduru RK, Darling KA, Kishore R, Scattergood RO, Koch CC, Murty KL. Evaluation of mechanical properties using shear–punch testing. Mater Sci Eng, A Mar. 2005;395(1–2):307–14. https://doi.org/10.1016/j.msea.2004.12.048.
[18] Esfandyarpour MJ, Alizadeh R, Mahmudi R. Applicability of shear punch testing to the evaluation of hot tensile deformation parameters and constitutive analyses. J Mater Res Technol Jan. 2019;8(1):996–1002. https://doi.org/10.1016/j.jmrt.2018.02.014.
[19] Kobayashi T, Miura Y, Yamamoto M. Tensile property evaluation of a Japanese reactor pressure vessel steel by Shear punch test technique. In: Lancaster R, Jeffs S, editors. Proceedings of the 5th international small scale test techniques (SSTT) conference. Swansea; 2018.
[20] Tang Y, Campbell J, Burley M, Dean J, Reed R, Clyne T. Profilometry-based indentation plastometry to obtain stress-strain curves from anisotropic superalloy components made by additive manufacturing. Materialia (Oxf) Mar. 2021;15:101017. https://doi.org/10.1016/j.mtla.2021.101017.
[21] Oliver WC, Pharr GM. An improved technique for determining hardness and elastic modulus using load and displacement sensing indentation experiments. J Mater Res Jun. 1992;7(6):1564–83. https://doi.org/10.1557/JMR.1992.1564.
[22] Suresh S, Giannakopoulos AE. A new method for estimating residual stresses by instrumented sharp indentation. Acta Mater Oct. 1998;46(16):5755–67. https://doi.org/10.1016/S1359-6454(98)00226-2.
[23] Chen L, Du Q, Yu M, Guo X, Zhao W. Measuring the effect of residual stress on the machined subsurface of Inconel 718 by nanoindentation. PLoS One Jan. 2021;16(1):e0245391. https://doi.org/10.1371/journal.pone.0245391.
[24] Wang H, Dhiman A, Ostergaard HE, Zhang Y, Siegmund T, Kruzic JJ, et al. Nanoindentation based properties of Inconel 718 at elevated temperatures: a comparison of conventional versus additively manufactured samples. Int J Plast Sep. 2019;120:380–94. https://doi.org/10.1016/j.ijplas.2019.04.018.
[25] Rifat M, Pagan DC, DeMeter EC, Basu S. On the formation of pileups during nano-scratching of Inconel 718 produced using additive manufacturing. Materialia (Oxf) Aug. 2023;30:101813. https://doi.org/10.1016/j.mtla.2023.101813.
[26] ASTM E8-04 standard test methods for tension testing of metallic materials. ASTM; 2010.
[27] EN 10371. Metallic materials - small punch test method," EN. 2021. 2021.
[28] "ASTM e3205-20 standard test method for small punch testing of metallic materials. ASTM; 2020.
[29] Tang YT, Campbell JE, Burley M, Reed RC, Clyne T. Use of profilometry-based indentation plastometry to obtain stress-strain curves from small superalloy components made by additive manufacturing. SSRN Electron J 2020. https://doi.org/10.2139/ssrn.3746800.
[30] Campbell JE, Thompson RP, Dean J, Clyne TW. Comparison between stress-strain plots obtained from indentation plastometry, based on residual indent profiles, and from uniaxial testing. Acta Mater Apr. 2019;168:87–99. https://doi.org/10.1016/j.actamat.2019.02.006.
[31] Campbell JE, Thompson RP, Dean J, Clyne TW. Experimental and computational issues for automated extraction of plasticity parameters from spherical indentation. Mech Mater Sep. 2018;124:118–31. https://doi.org/10.1016/j.mechmat.2018.06.004.
[32] ASTM, "ASTM. E2546-07 standard practice for instrumented indentation testing. West Conshohocken, PA: ASTM International; 2015.
[33] Kañetas PJP, Calvo J, Rodriguez-Calvillo P, Cabrera Marrero JM, Zamora Antuñano MA, Guerrero-Mata MP. EBSD study of delta-processed Ni-based superalloy. Metals Nov. 2020;10(11):1466. https://doi.org/10.3390/met10111466.
[34] Chen B-R, Yeh A-C, Yeh J-W. Effect of one-step recrystallization on the grain boundary evolution of CoCrFeMnNi high entropy alloy and its subsystems. Sci Rep Mar. 2016;6(1):22306. https://doi.org/10.1038/srep22306.

[35] Ferreri NC, Vogel SC, Knezevic M. Determining volume fractions of γ, γ′, γ″, δ, and MC-carbide phases in Inconel 718 as a function of its processing history using an advanced neutron diffraction procedure,". Mater Sci Eng, A Apr. 2020;781:139228. https://doi.org/10.1016/j.msea.2020.139228.

[36] Dehmas M, Lacaze J, Niang A, Viguier B. TEM study of high-temperature precipitation of delta phase in Inconel 718 alloy. Adv Mater Sci Eng 2011;2011:1–9. https://doi.org/10.1155/2011/940634.

[37] Ferreri NC, Vogel SC, Knezevic M. Determining volume fractions of γ, γ′, γ″, δ, and MC-carbide phases in Inconel 718 as a function of its processing history using an advanced neutron diffraction procedure,". Mater Sci Eng, A Apr. 2020;781:139228. https://doi.org/10.1016/j.msea.2020.139228.

[38] Hosseini E, Popovich VA. A review of mechanical properties of additively manufactured Inconel 718. Addit Manuf Dec. 2019;30:100877. https://doi.org/10.1016/j.addma.2019.100877.

[39] Schröder J, Evans A, Polatidis E, Capek J, Mohr G, Serrano-Munoz I, et al. Understanding the impact of texture on the micromechanical anisotropy of laser powder bed fused Inconel 718. J Mater Sci Aug. 2022;57(31):15036–58. https://doi.org/10.1007/s10853-022-07499-9.

[40] Kindermann RM, Roy MJ, Morana R, Francis JA. Effects of microstructural heterogeneity and structural defects on the mechanical behaviour of wire + arc additively manufactured Inconel 718 components. Mater Sci Eng, A Apr. 2022;839:142826. https://doi.org/10.1016/j.msea.2022.142826.

[41] Zhang P, Li SX, Zhang ZF. General relationship between strength and hardness. Mater Sci Eng, A Nov. 2011;529:62–73. https://doi.org/10.1016/j.msea.2011.08.061.

[42] Pintaude G. Hardness as an indicator of material strength: a critical review. Crit Rev Solid State Mater Sci Jun. 2022:1–19. https://doi.org/10.1080/10408436.2022.2085659.

[43] Tabor D. The hardness of metals. Oxford University Press; 2000.

[44] Voyiadjis GZ, Almasri AH. Variable material length scale associated with nanoindentation experiments. J Eng Mech Mar. 2009;135(3):139–48. https://doi.org/10.1061/(ASCE)0733-9399.

[45] V Kontomaris S, Stylianou A, Malamou A, Nikita KS. An alternative approach for the Young's modulus determination of biological samples regarding AFM indentation experiments. Mater Res Express Nov. 2018;6(2):025407. https://doi.org/10.1088/2053-1591/aaef10.